ARTICLE IN PRESS

S0997-7546(02)01205-0/FLA   AID:1205   Vol.●●●(●●●)
ELSGMLTM(EJMFLU):m4SC 2002/08/30 Prn:4/09/2002; 14:54

ejmflu1205

P.1(1-15)
by:CG p. 1

Investigations of time-growing instabilities in laminar separation bubbles

Ulrich Rist [*], Ulrich Maucher

Institut für Aerodynamik & Gasdynamik, Universität Stuttgart, Pfaffenwaldring 21, D-70550 Stuttgart, Germany

Abstract

The occurrence of temporally growing unstable disturbances is investigated based on eigenvalues with zero group velocity from linear stability theory (LST) and compared with observations of upstream travelling disturbances obtained in a two-dimensional direct numerical simulation (DNS) of an unsteady laminar separation bubble. Numerical solutions of the Orr–Sommerfeld equation using analytically constructed base-flow velocity profiles modelled by a modified hyperbolic tangent function help to identify the role of parameters, such as maximum reverse flow, wall distance and intensity of the shear layer, as well as Reynolds number on the possibility that a true time-growing instability occurs. Then, the viscous or inviscid nature of the solutions found is classified on the basis of their eigenfunctions. For large wall distances two unstable modes are found. Apart from a low-frequency motion of the bubble the DNS exhibit high-frequency oscillations which periodically appear and disappear. Part of these disturbances travel upstream and amplify with respect to time. Their initial occurrence and their frequency are in excellent agreement with the results of the parameter study based on LST and a closer examination of the disturbances yields insight into their spatial structure.
© 2002 Éditions scientifiques et médicales Elsevier SAS. All rights reserved.

Keywords: Laminar separation bubble; Absolute and convective instability; Direct numerical simulation

1. Introduction

Typically, a laminar boundary layer separates from the wall already under the influence of a rather mild adverse stream-wise pressure gradient. Flow instability leads to transition and, if the wall is not too far away, to turbulent re-attachment of the flow, thus creating a so-called laminar separation bubble (termed LSB from here on). Early experimental research has focused on establishing empirical laws for the prediction of the size of LSBs based on local flow properties, such as some Reynolds number at separation or mean-pressure gradients, for instance (cf. Tani [1], Gaster [2], van Ingen [3]). Despite continuous research a generally applicable method has not been found yet, most probably because of insufficient knowledge about the laminar-turbulent transition process in LSBs.

Based on experimental evidence and on direct numerical simulations (DNS) of LSBs (e.g., Pauley et al. [4], Spalart and Strelets [5], Yang and Voke [6]) the common view shared by many investigators is that transition in a LSB develops from some inherent shear-layer or "Kelvin–Helmholtz instability" which depends primarily on local properties and not on disturbances coming from upstream. Unfortunately, in most cases the incoming disturbances are not very well documented (if at all) and their initial amplitudes, spectra and wall-normal profiles are not known. Because of the large amplification rates prior to, as well as within the LSB initially small convective disturbances may play a role at transition and disturbance amplitudes of the order of $u'_{rms} \approx 10^{-4}$ upstream of the LSB must be considered as 'high'. Consequently, it is unclear whether a transition is caused

---

[*] Correspondence and reprints.
   E-mail address: rist@iag.uni-stuttgart.de (U. Rist).

by convective amplification of already large disturbances or merely by a so-called absolute instability in the vicinity of the reattachment zone (Gaster [7], Allen and Riley [8]). Such an issue can only be clarified in a theoretical or a numerical approach where initial disturbances can be reduced to much lower levels than in a laboratory experiment, if not completely eliminated. However, such investigations suffer from problems like linearisation of the governing equations, local approximations like the parallel-flow assumption, and, especially in the present case, from the need to assume certain disturbance-free base-flow velocity profiles, since these cannot be computed directly if an absolute instability is present.

Nevertheless, several papers exist where base-flow profiles have been approximated by different analytical functions or solutions of modified differential equations (Michalke [9], Gaster [7], Allen and Riley [8], Hammond and Redekopp [10] and Alam and Sandham [11], for instance) in order to contribute to the issue using linear stability theory (LST). Based on these investigations it appears that relatively large back-flow intensities on the order of 15–20% relative to the free-stream velocity are needed before an absolutely unstable mode can be found.

DNS on the other hand, should be able to provide further evidence or insight. The transition mechanism identified by Spalart and Strelets [5], for instance, involves a "*wavering (flapping) of the shear layer and then Kelvin–Helmholtz vortices, which instantly become three-dimensional without pairing*". This sounds as if an absolute instability were present but the mean-flow profiles do not meet with the back-flow criterion given above. Instead, some "spontaneous transition" based on upstream propagating disturbances, reflections and receptivity is assumed. This view is also supported by accompanying RANS-computations which are rather successful. However, without further evaluation of the data and a spectral decomposition of the disturbances a further insight cannot be obtained.

Another open issue is the influence of the wall on the instability of the detached boundary layer in comparison to a free shear layer. Recent experiments (Watmuff [12]) and DNS show a very close resemblance to a free-shear-layer instability. However, the occurrence of Λ-structures (cf. Alam and Sandham [11] or Watmuff [12]) indicates a yet unknown contribution of the wall, since such structures are typically not observed in a true free-shear-layer transition. Also, Rist et al. [13,14] have observed a less dominant role of secondary instability (leading to Λ-vortices) than in attached boundary layers, as well as a damping influence on the shear-layer instability by the presence of the wall. In these cases an absolute instability was clearly ruled out by switching the disturbance generator off and observing the flow to become steady. But this could have been biased by a too weak back-flow intensity, too low Reynolds number or a too weak pressure gradient. Therefore, the present paper concentrates on the investigation of such parameters as reverse-flow velocity, wall distance, intensity of the shear layer, and local Reynolds number on a possible absolute instability via examination of time-growing instabilities which are not convected away. The underlying analytical base-flow profiles are presented in Section 2.1, typical results in Section 2.2, and the occurrence of two unstable modes in Section 2.3. More results of these investigations can be found in Maucher [15]. Results of a two-dimensional DNS with a large separation bubble in an extremely small disturbance environment are discussed in Section 3 and compared to the results of Section 2. The paper ends with the conclusions in Section 4.

2. Linear stability calculations

The calculations presented in this section are based on the usual assumptions for LST of incompressible fluids: parallel-flow approximation, small-amplitude disturbances and normal disturbance modes, i.e.,

$$u(x, y, t) = U(y) + \varepsilon A_u(y) \cos[\alpha x - \beta t - \theta_u(y)], \tag{1}$$

$$v(x, y, t) = \varepsilon A_v(y) \cos[\alpha x - \beta t - \theta_v(y)], \tag{2}$$

where x, y, and t are the streamwise coordinate, the wall-normal coordinate, and time, respectively. The corresponding velocity components have been designated by u and v, as usual. A_u, A_v, θ_u, and θ_v are their respective amplitudes and phases. Linearisation of the Navier–Stokes equations with respect to the small disturbance amplitude ε leads to the well-known Orr–Sommerfeld equation (cf. White [16]). After discretisation of the y-derivatives using sixth-order accurate finite differences on a fine grid this can be solved as an eigenvalue problem for either the streamwise wave number α or the frequency β (depending on the choice which of the two is prescribed by the user). For the present investigations we follow Gaster [17] who has investigated and interpreted the tangled behaviour of the eigenvalues of the Orr–Sommerfeld equation. Both wave numbers α and β must be treated as complex numbers and the group velocity

$$c_g = \frac{\partial \beta}{\partial \alpha} \tag{3}$$

must be considered. Gaster concludes that "*where modes with zero group velocity exist, the energy is not convected away from the source and there is the possibility of a true time-growing instability.*" For the present investigations this is implemented as

$$c_g = 0 \quad \text{and} \quad \beta_i > 0. \tag{4}$$

ARTICLE IN PRESS

S0997-7546(02)01205-0/FLA   AID:1205   Vol.●●●(●●●)
ELSGMLTM(EJMFLU):m4SC 2002/08/30 Prn:4/09/2002; 14:54

ejmflu1205

P.3 (1-15)
by:CG p. 3

U. Rist, U. Maucher / European Journal of Mechanics B/Fluids ●●● (●●●●) ●●●–●●●   3

The computer code to solve the Orr–Sommerfeld equation has been implemented as a so-called "shooting method" which solves for the most unstable eigenvalue. For either real frequency β or real streamwise wave number α it has been verified by comparisons with a "matrix method" which computes every eigenvalue (including the so-called discrete spectrum) as well as with DNS. Since it has been used without major problems for a decade now we felt confident to use it for the present investigations as well. Starting from a known eigenvalue (or close to it) the 4-D space which is spanned by α_r, α_i, β_r, and β_i can be investigated for a certain base-flow profile $U(y)$ and Reynolds number $Re_{\delta_1} = U_e \delta_1 / \nu$, where U_e is the boundary layer edge velocity and δ_1 the displacement thickness. Once a few eigenvalues are known, the group velocity can be easily computed by (finite-difference) differentiation of the eigenvalues. The code then automatically searches for the eigenvalues with zero group velocity.

2.1. Analytical base-flow profiles

As already mentioned in the introduction, it is hardly possible to directly compute absolutely unstable velocity profiles [$U(y)$ in Eq. (1)] from the full Navier–Stokes equations because of the problem that numerical errors will be picked up and amplified by the instability until a solution is found that includes nonlinear effects of the instability. This is avoided using analytical functions which resemble velocity profiles in a separation bubble. Here we use

$$U(y) = \tanh\{a[y - h_R - (y - h_R)^r]\}, \tag{5}$$

which offers the advantage that the influence of several parameters describing the flow can be investigated more clearly. Apart from the Reynolds number Re_{δ_1}, these are the maximum back-flow intensity U_R, some measure for the distance of the shear-layer from the wall h_R or the maximum shear of the detached shear layer ω_{max}. Here h_R is chosen, defined as the wall distance where $U(y)$ is zero (which is closer to the wall than the separation stream line or the inflection point of $U(y)$). To compute $U(y)$ the constant a

$$a = \frac{1}{2} \frac{\log((1 - U_R)/(1 + U_R))}{(1/r)^{1/(r-1)} - (1/r)^{r/(r-1)}} \tag{6}$$

and the exponent r are iterated for a specified U_R until the desired h_R is reached. Typical examples of base-flow profiles are shown in Fig. 1 for several parameters of U_R and h_R. Increasing the reverse-flow intensity leads to an increasingly large reverse-shear layer at the wall because of the no-slip condition while the maximum shear in the free shear layer is only slightly increased. Thus, it can be expected that the main influence of the reverse flow on the linear flow instability is through the differences near the wall which are of viscous nature and hence Reynolds number dependent. On the other hand, larger wall distances increase the free shear layer maximum and decrease the wall shear so that the instability of such profiles should be dominated by free shear layer effects, which are of inviscid nature.

Gaster [7] found that a reverse-flow profile with $U_R = 14.5\%$ is at the edge of absolute instability. His corresponding profile is compared to the present family of profiles in Fig. 2. For $h_R/\delta_1 = 0.6$ close visual agreement is observed. However, small discrepancies between the profiles lead to somewhat larger differences in the eigenvalues, e.g., $\delta_1 \cdot \beta_i = -0.059$ for the profiles from Eq. (5) instead of $\delta_1 \cdot \beta_i = -0.009$ as for Gaster's profile using our LST code. This corresponds to a difference of about 15% compared to the largest (positive) temporal amplification rate found in the present investigations. Most probably,
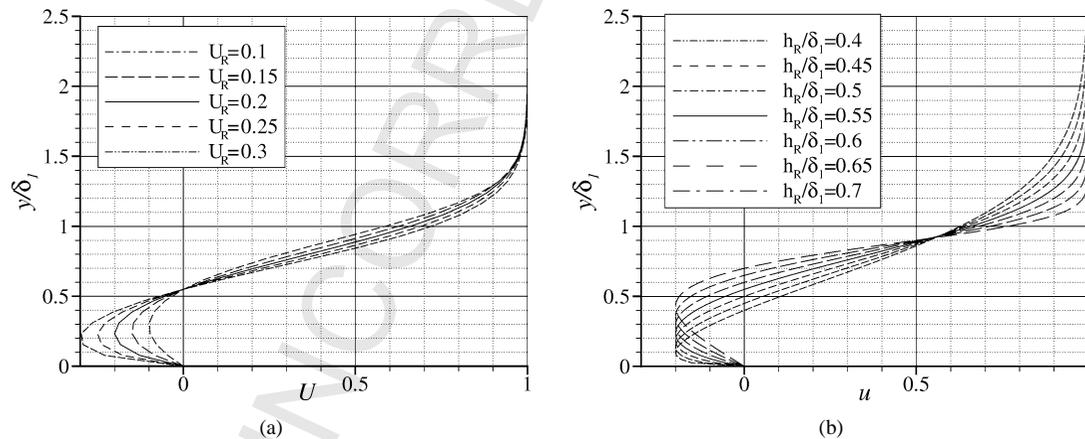

Fig. 1. Examples of analytical velocity profiles. (a) Variation of the reverse-flow intensity U_R for constant wall distance $h_R/\delta_1 = 0.55$ of the separated layer; (b) variation of the height for constant reverse flow $U_R = -0.2$.
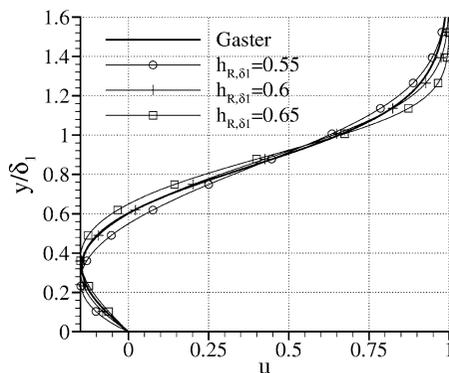
ARTICLE IN PRESS

S0997-7546(02)01205-0/FLA AID:1205 Vol.●●●(●●●)
ELSGMLTM(EJMFLU):m4SC 2002/08/30 Prn:4/09/2002; 14:54

ejmflu1205

P.4 (1-15)
by:CG p. 4

4   *U. Rist, U. Maucher / European Journal of Mechanics B/Fluids ●●● (●●●●) ●●●–●●●*

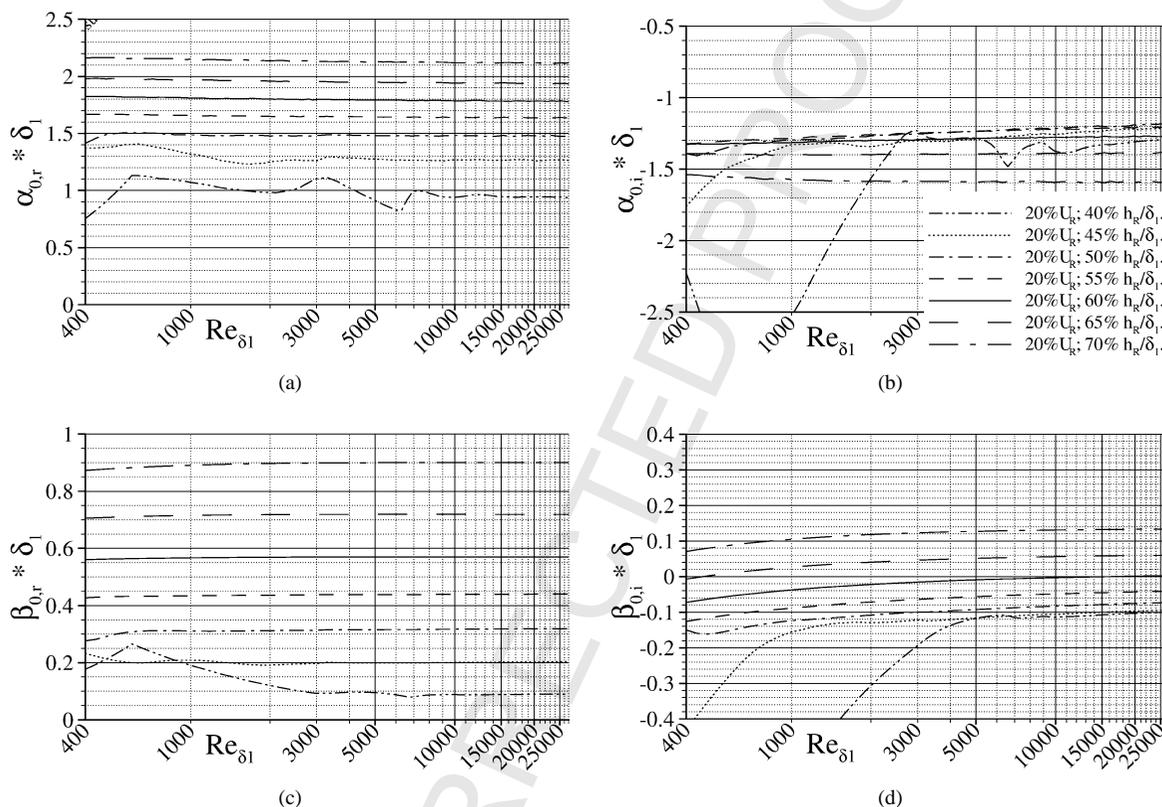Fig. 2. Comparison with a base flow profile by Gaster [7] ($C = 0.6$, $U_R = 0.145$).

(a)   (b)

(c)   (d)

Fig. 3. Eigenvalues with zero group velocity for $U_R = 0.20$, $\alpha_{0,r}$ (a), $\alpha_{0,i}$ (b), $\beta_{0,r}$ (c), $\beta_{0,i}$ (d).

such a quantitative agreement is good enough for the following examinations regarding the analytical (and hence somewhat arbitrary) character of the velocity profiles used in these and other investigations compared to (unfortunately not well defined) 'real' flows.

2.2. Influence of Reynolds number, wall distance and reverse flow

Results for the variation of Re_{δ_1} and h_R for constant $U_R = 0.20$ are shown in Fig. 3.[1] Apparently, the influence of the Reynolds number on the eigenvalues is confined to $Re_{\delta_1} < 5000$ and $h_R < 0.5\,\delta_1$ in accordance with the discussion of the base-

---

[1] Double indices $(0, r/i)$ are used to remind the reader that only modes with $c_g = 0$ are considered.

flow profiles above. Generally, larger wall distances lead to smaller streamwise scales (i.e., larger wave number α_r), higher frequency β_r, as well as larger spatial and temporal amplification. Note that all eigenvalues shown exhibit rather large spatial downstream growth because $\alpha_i < 0$. However, a time-growing instability ($\beta_i > 0$) can only be expected for the two profiles with the largest wall distance of the shear layer (i.e., $h_R/\delta_1 = 0.65$ and 0.70) despite the fact that $U_R = 0.2$ is larger than the limit $U_R = 0.145$ for absolute instability given by Gaster [7]. Since the maximum shear in the corresponding base-flow profiles is largest, this could also be understood as an effect of increasing shear-layer strength. In any case, the present results demonstrate that more parameters than the maximum reverse flow strength or Reynolds number must be considered to adequately describe the problem.

A look at the eigenfunctions in Fig. 4 explains why the Reynolds number has a less pronounced effect on the instability of the profiles with larger h_R. The u-eigenfunctions for the largest wall distance resemble those of a free-shear-layer instability very closely, apart from a Stokes layer at the wall which is Reynolds number dependent. Here, the instability is practically inviscid since Reynolds number effects are confined to the less dominant wall shear layer. However, for a smaller wall distance-parameter h_R as in Fig. 4(b) the instability changes towards a viscous instability which is characterized by Tollmien–Schlichting-type eigenfunctions together with a larger Reynolds number dependence. The figure demonstrates that an inviscid *free shear layer type instability* can be distinguished from a viscous *wall-mode instability* by the position and the relative strength of the eigenfunction maxima.

The influence of the reverse-flow velocity in the present profiles is to move the instability from one type to the next: the wall shear increases with growing U_R in Fig. 5 and the amplitudes close to the wall rise over those in the detached shear layer. This could be already expected from the discussion of the characteristics of the base-flow profiles in connection with Fig. 1. All cases shown are dominated by the wall mode because of the shear layer at the wall, especially when that one is very large, as for $U_R = 0.30$. Reducing U_R has the effect of reducing the wall shear layer with respect to the free shear layer with the consequence that the inviscid type of instability plays a more pronounced role.

Coming back to the eigenvalues again, the general effect of reducing the reverse flow is to decrease α_r and α_i, to increase the frequency β_r and to reduce the temporal amplification rate β_i. Increasing the back flow has the contrary effect. All this can be deduced from the 3-D representations in Fig. 6 which summarize the present investigations performed in the region

$$400 \leqslant Re_{\delta_1} \leqslant 25000, \qquad 0.1 \leqslant U_R \leqslant 0.3, \qquad 0.4 \leqslant \frac{h_R}{\delta_1} \leqslant 0.7. \tag{7}$$

Oscillations at the lowest Reynolds number indicate the transition between the two instability types and occasional holes are due to some convergence problems of the LST solver when searching for the second unstable eigenmode described in the next section. From Fig. 6(d) it is clear that the most unstable modes with $\beta_i > 0$ must be expected in the corner where all three parameters are largest, and that reducing every one of the three reduces time-growing instability. However, there occurs a second instability region in the lower far-side corner of the domain, which will be discussed further in the next section.
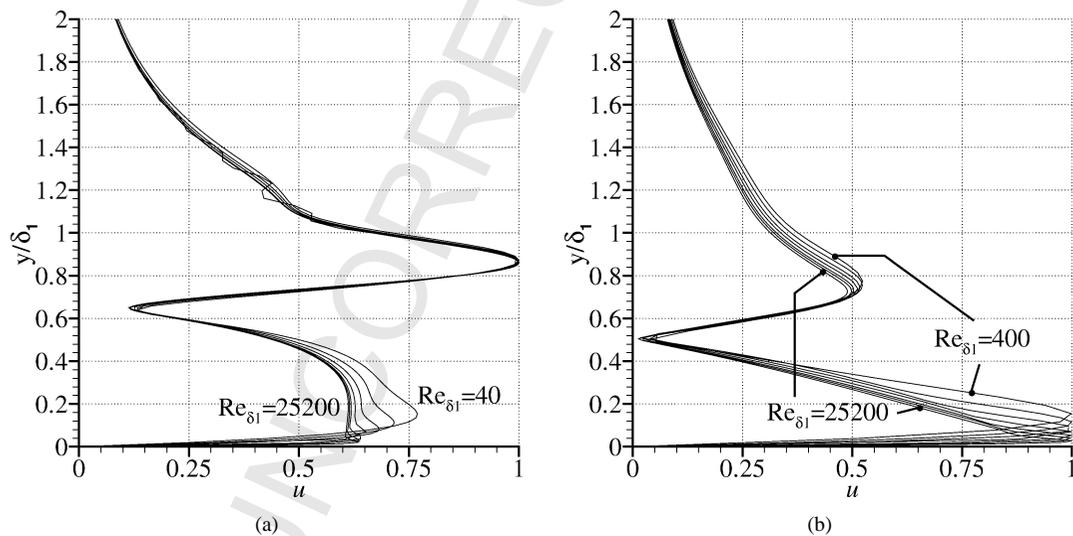

Fig. 4. Effect of changing the Reynolds number and wall-distance of the shear layer for $U_R = 0.2$, $h_R/\delta_1 = 0.70$ (a) and $h_R/\delta_1 = 0.55$ (b).
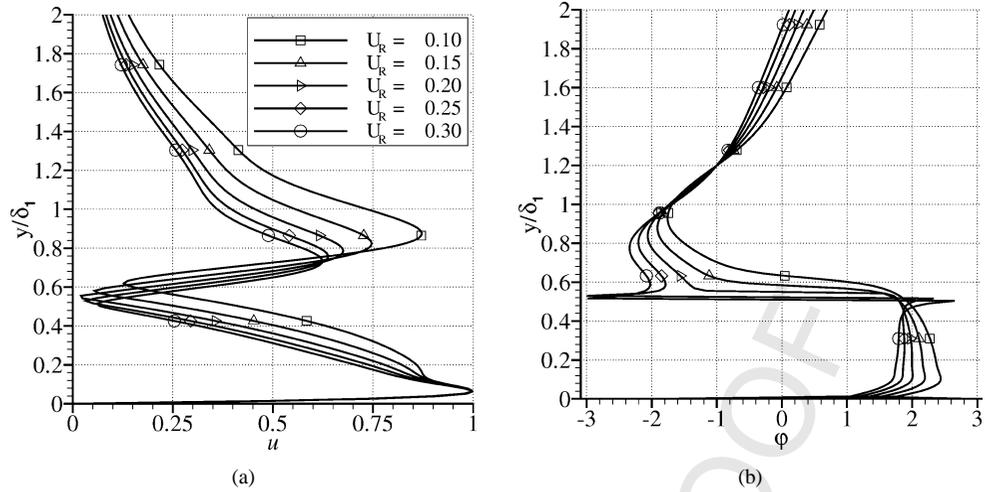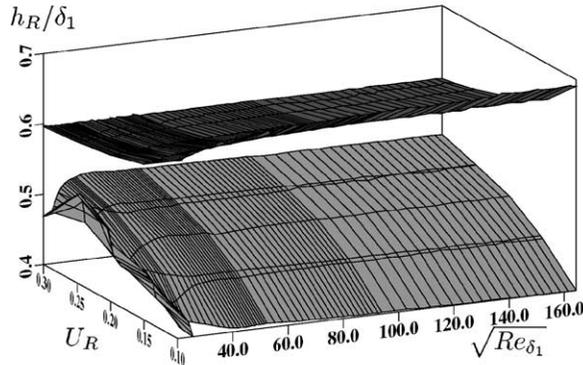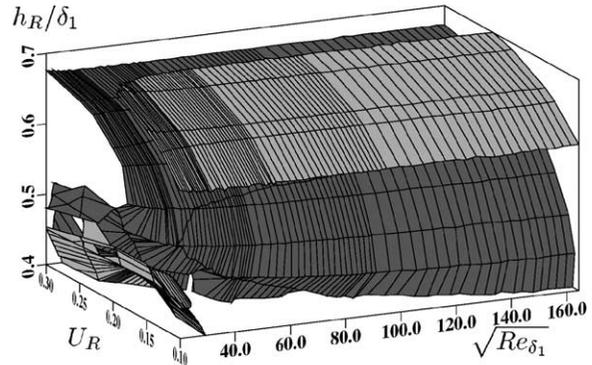
ARTICLE IN PRESS

S0997-7546(02)01205-0/FLA   AID:1205   Vol.●●●(●●●)
ELSGMLTM(EJMFLU):m4SC 2002/08/30 Prn:4/09/2002; 14:54

ejmflu1205

P.6 (1-15)
by:CG p. 6

6   *U. Rist, U. Maucher / European Journal of Mechanics B/Fluids ●●● (●●●●) ●●●–●●●*

(a)   (b)

Fig. 5. Effect of changing the reverse flow intensity at $h_R/\delta_1 = 0.6$, $Re_{\delta_1} = 3000$. (a) amplitudes, and (b) phases of u-eigenfunction.
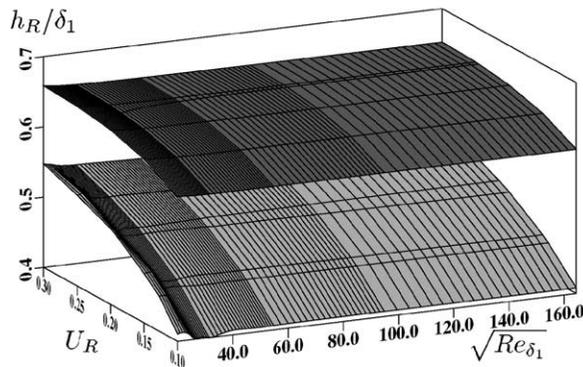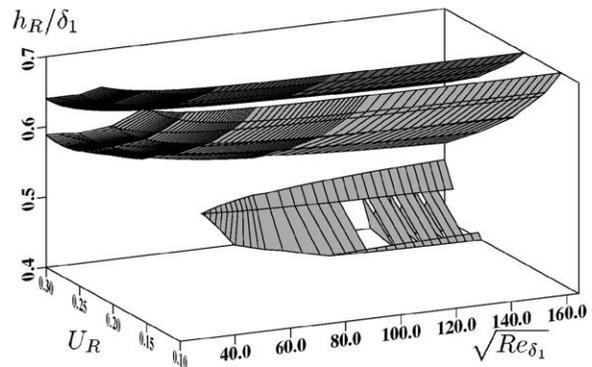

Fig. 6. Eigenvalues with zero group velocity. Iso-surfaces of $\alpha_{0,r}$ (a), $\alpha_{0,i}$ (b), $\beta_{0,r}$ (c), and $\beta_{0,i}$ (d).

2.3. Multiple modes

Since the shooting method may converge to different eigenvalues depending on the initial conditions used, it is possible to find different eigenvalues for the same set of parameters determined by the path chosen to march from one solution to the

ARTICLE IN PRESS

S0997-7546(02)01205-0/FLA   AID:1205   Vol.●●●(●●●)
ELSGMLTM(EJMFLU):m4SC 2002/08/30 Prn:4/09/2002; 14:54

ejmflu1205

P.7 (1-15)
by:CG p. 7

U. Rist, U. Maucher / European Journal of Mechanics B/Fluids ●●● (●●●●) ●●●–●●●

7

next. In such a way, the second unstable eigenvalues shown in Fig. 6(d) have been detected. Their behaviour with respect to a variation of the parameter h_R is compared in Fig. 7 for $Re_{\delta_1} = 9000$ and $U_R = 0.3$.

They appear as two distinct modes. Typically, the newly observed mode ② has larger wave number α_r and hence shorter streamwise wave length, as well as a larger frequency than the mode ① discussed so far. For wall distances of the shear layer larger than $h_R/\delta_1 \approx 0.525$ mode ② becomes more interesting because of its larger spatial and temporal amplification rates, as well as its finite streamwise wave number α_r: α_r of mode ① tends towards zero which means that its streamwise wave length becomes increasingly larger, perhaps too large for a local analysis using the parallel-flow assumption. Therefore, the occurrence of mode ② seems to be more likely for large wall distances.

A comparison of the eigenfunctions of the two modes in Fig. 8 shows further differences. Mode ① exhibits the typical shear-layer maxima which increase with increasing h_R. However, the newly found mode ② is dominated by viscous wall effects, at least for the present Reynolds number. This indicates that this mode stems from the reverse flow at the wall which is similar to a wall jet in the upstream direction.
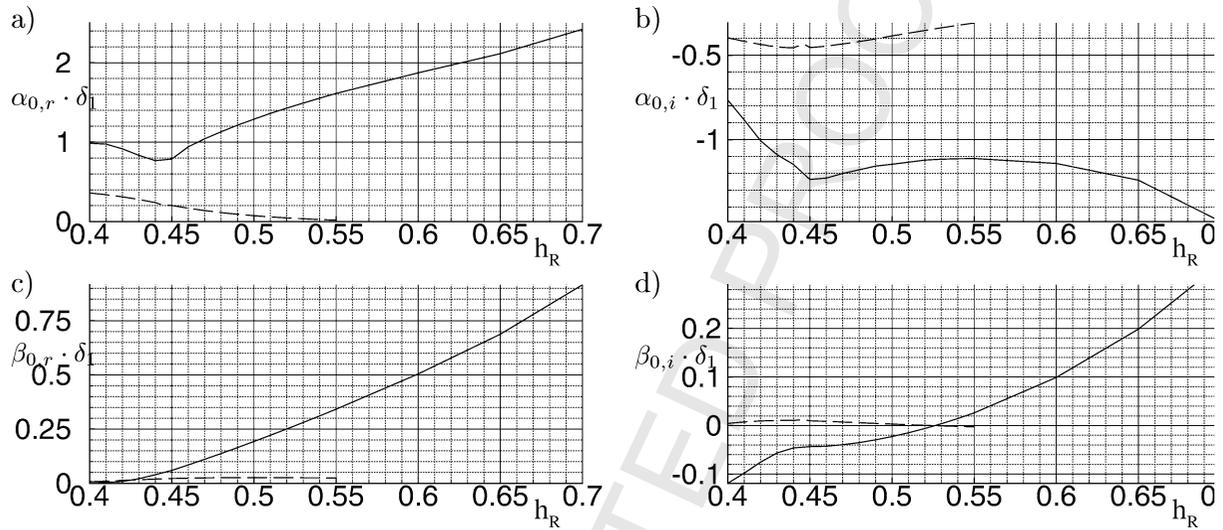

Fig. 7. Eigenvalues of mode ① and ② (dashed and solid, resp.) at $Re_{\delta_1} = 9000$ and $U_R = 0.3$: α_r (a), α_i (b), β_r (c), β_i (d).
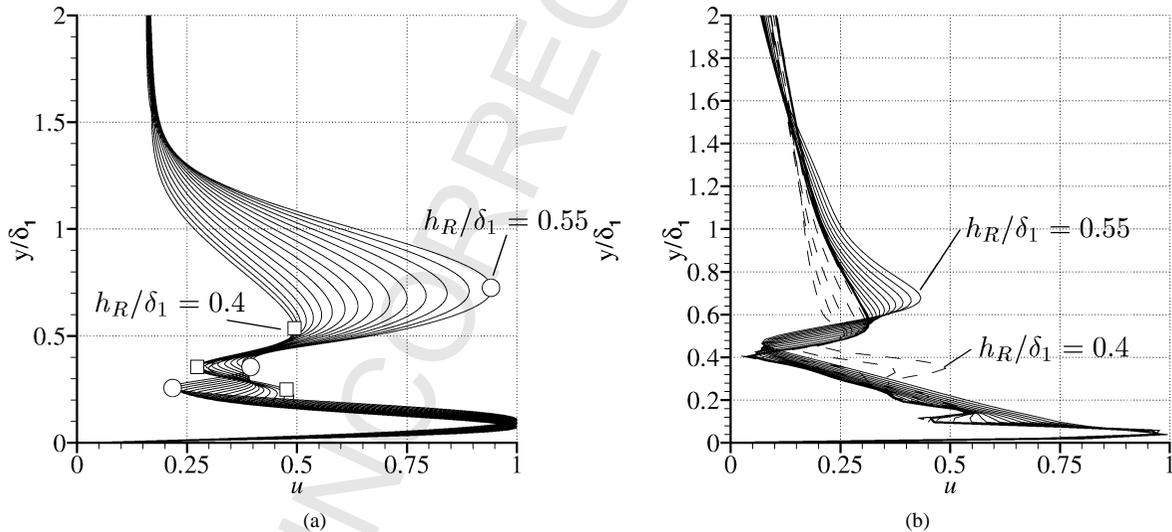

Fig. 8. Comparison of the u-eigenfunction for mode ① (a) and ② (b) for $U_R = 0.3$, $Re_{\delta_1} = 9000$, and $0.4 < h_R/\delta_1 < 0.55$; $h_R/\delta_1 = 0.45$ fat in (b).

ARTICLE IN PRESS

S0997-7546(02)01205-0/FLA AID:1205 Vol.●●●(●●●)
ELSGMLTM(EJMFLU):m4SC 2002/08/30 Prn:4/09/2002; 14:54   ejmflu1205   P.8 (1-15)
by:CG p. 8

8   *U. Rist, U. Maucher / European Journal of Mechanics B/Fluids ●●● (●●●●) ●●●–●●●*

3. Observations in direct numerical simulations

The present DNS investigations are for a two-dimensional flow only. Results of three-dimensional investigations can be found in Rist and Maucher [13], Rist et al. [14], Maucher et al. [18] or Maucher et al. [19], for instance. The scheme described in Rist and Fasel [20] has been adapted according to the procedure already used by Gruber et al. [21], see Fig. 9: a Blasius boundary layer with $Re_{\delta_1} = 1244$ is prescribed at the inflow boundary A–B where the height of the integration domain corresponds to $17.5\,\delta_1$. The free-stream velocity component $U_e(x)$ is prescribed along the boundary B–C of the integration domain, together with zero vorticity and $\partial v/\partial y = -dU_e/dx$ for the wall-normal velocity component. Here, a long constant U_e is followed by a deceleration by -7.5% relative to U_e at inflow followed by an accelerated Falkner–Skan boundary layer within the buffer zone. Compared to an experiment on an FX66-S-196 airfoil at $9°$ angle of attack ($U_\infty = 30.3$m/s, $Re_{\text{chord}} = 1.5 \cdot 10^6$) the adverse pressure gradient thus created is weaker but still high enough to cause massive unsteady separation effects downstream of $x \approx 3$ as will be shown further down. Note: the experimental velocity is for a turbulent boundary layer caused by roughness elements which suppress the separation bubble in order to show the "inviscid velocity ramp". Compared to the experiment the present results are normalized with U_∞ and $L = 7.4$ cm as reference length.

The numerical method solves the vorticity transport equation by an explicit fourth-order accurate finite-difference scheme followed by an iterative solution of a Poisson equation for the wall-normal velocity component v which is accelerated by a multi-grid procedure using four grids and several V-cycles. The instantaneous wall-parallel velocity component u is obtained by integrating the continuity equation throughout the integration domain. At the wall $u = v = 0$ and $\partial \omega/\partial x = -\partial^2 v/\partial y^2$ are used as boundary conditions. At outflow the "relaminarization zone technique" by Kloker et al. [22] is used as a buffer domain to ramp the instantaneous vorticity towards the steady vorticity of a Falkner–Skan boundary layer. The velocity components adjust themselves without additional forcing and the velocity disturbances u' and v' decay towards the outflow boundary to extremely small values. Therefore, the condition $\partial^2 v/\partial x^2$ is sufficient at the outflow. In fact, the inflow and the free-stream boundary conditions are perfectly steady.

In the first simulations using this set-up and 4 V-cycles as in Rist and Fasel [20] periodic oscillations with a normalized circular frequency $\beta_0 \approx 20$ occurred (Maucher et al. [23]), corresponding to a Strouhal number of $St = \beta_0 \delta_{2,s}/2\pi u_{e,s} = 0.0043$ which is somewhat different from the 'universal' Strouhal number ($St = 0.00686$) of Pauley et al. [4] but the qualitative features of the instantaneous flow field are the same (cf. Fig. 10).
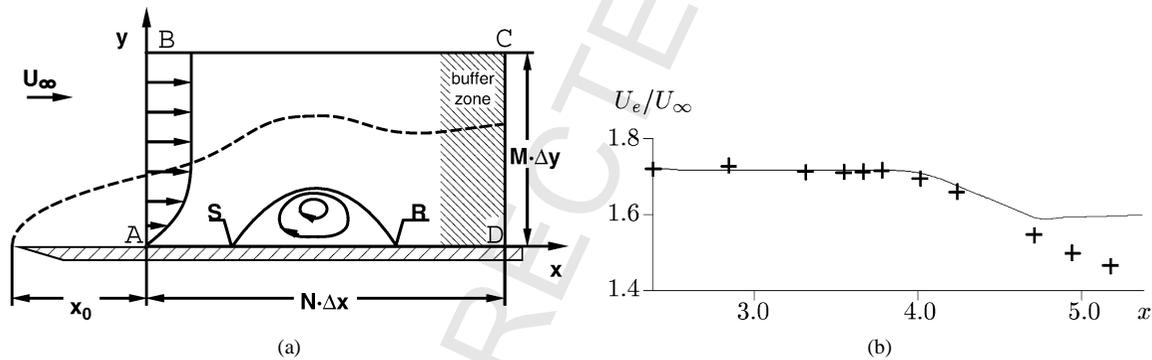

Fig. 9. Integration domain (a) and free-stream velocity (b) for the DNS of a laminar separation bubble. S = separation point, R = reattachment point; experimental measurements with tripped boundary layer (+) for comparison.
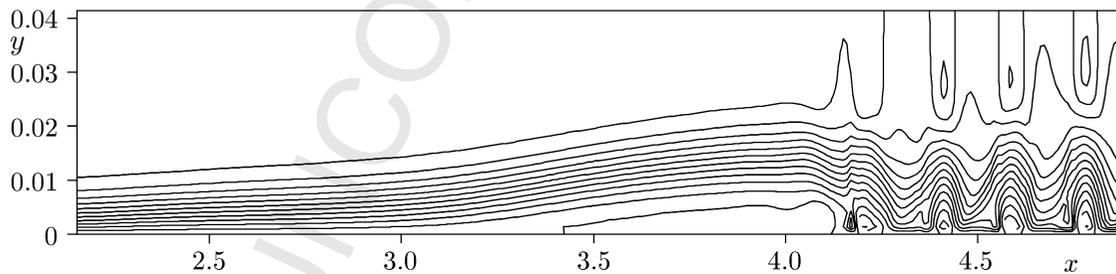

Fig. 10. Contours of instantaneous velocity from precursory simulation showing self-excited periodical vortex shedding.

ARTICLE IN PRESS

S0997-7546(02)01205-0/FLA   AID:1205   Vol.●●●(●●●)
ELSGMLTM(EJMFLU):m4SC 2002/08/30 Prn:4/09/2002; 14:54

ejmflu1205

P.9 (1-15)
by:CG p. 9

U. Rist, U. Maucher / European Journal of Mechanics B/Fluids ●●● (●●●●) ●●●—●●●   9

However, after doubling the number of V-cycles of the multi-grid procedure which solves the v-Poisson equation, in an effort to minimize the numerical errors, it was found that another kind of unsteadiness appears. The high-frequency oscillations are no longer periodic with respect to a single frequency, nor do they show a constant amplitude. Instead, they consist of a frequency band centred around the most unstable frequency according to LST which leads to spatial amplitude variations as can be seen in Fig. 11(a). For this and all subsequent pictures time is shown in multiples of $T_{\beta=30} = 0.209\,L/U_\infty$, which corresponds to the period of a (fictitious disturbance) frequency with $\beta = 30$, i.e., $f = 1955$ Hz.

An analysis of this result in Maucher [15] has shown that the disturbances arise from small-amplitude unsteadiness at the upstream end of the bubble via convective amplification according to LST. Towards the rearward end of the bubble they reach non-linear saturation (and become apparent in the instantaneous flow field). The transverse momentum added to the flow by the non-linear disturbances prevents the flow from separating again in the region of adverse pressure gradient (which starts at $x \approx 4$, cf. Fig. 9(b)). Because the amplification of disturbances is related to the presence of the bubble via its mean-flow velocity profiles which control the amplification rates, the disturbances decrease and finally die away together with the bubble. This change completely alters the picture: Now a quasi steady LSB appears in the region of adverse pressure gradient which starts to grow in size, cf. Fig. 11 (b) and (c). The first signs of renewed high-frequency activity are small oscillations within the bubble towards its rearward end, as can be seen in Fig. 11(c). Since the separation point is not fixed by a step, the bubble slowly moves further upstream into the region of constant pressure where it finally disappears. Again after a certain time delay the travelling wave-packets reappear, as before.

The overall picture of the present regime is that of an unsteady flow governed by two largely different time scales where the period of appearance of the LSB at a certain location is about 100 times larger than the average period of the high-frequency disturbances. Instantaneous velocity contours in Fig. 11 and time traces of the wall vorticity in Fig. 12 illustrate this behaviour quite well.

Clearly, the two smallest x-stations in Fig. 12 are in the region where the bubble periodically appears and disappears (negative vorticity means reverse flow near the wall). In the absence of any appreciable disturbances a long quasi-steady bubble develops until the sudden occurrence of high-frequency oscillations. These disturbances grow to very large amplitudes and the laminar separation bubble becomes smaller and moves upstream, as can be seen in the comparison of the time instants in Fig. 11.
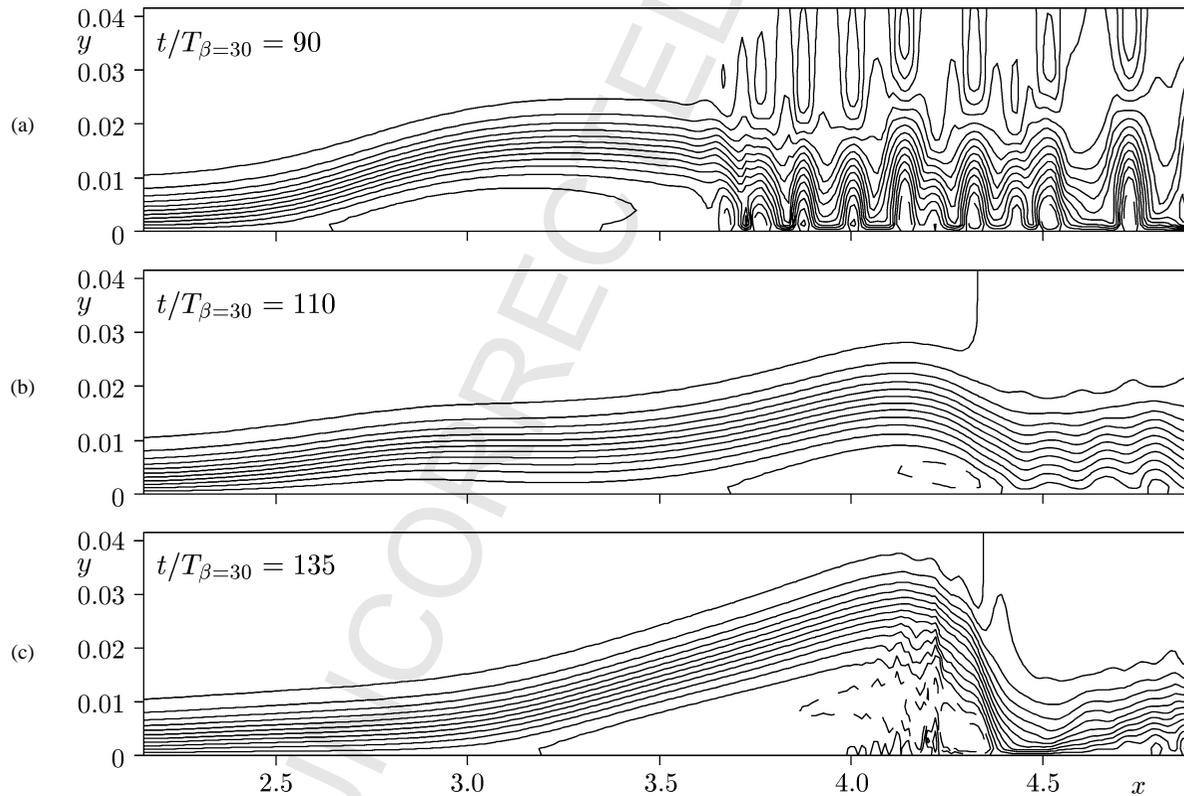

Fig. 11. Instantaneous velocity at $t/T_{\beta=30} = 90$ (a), $t/T_{\beta=30} = 110$ (b), and $t/T_{\beta=30} = 135$ (c).
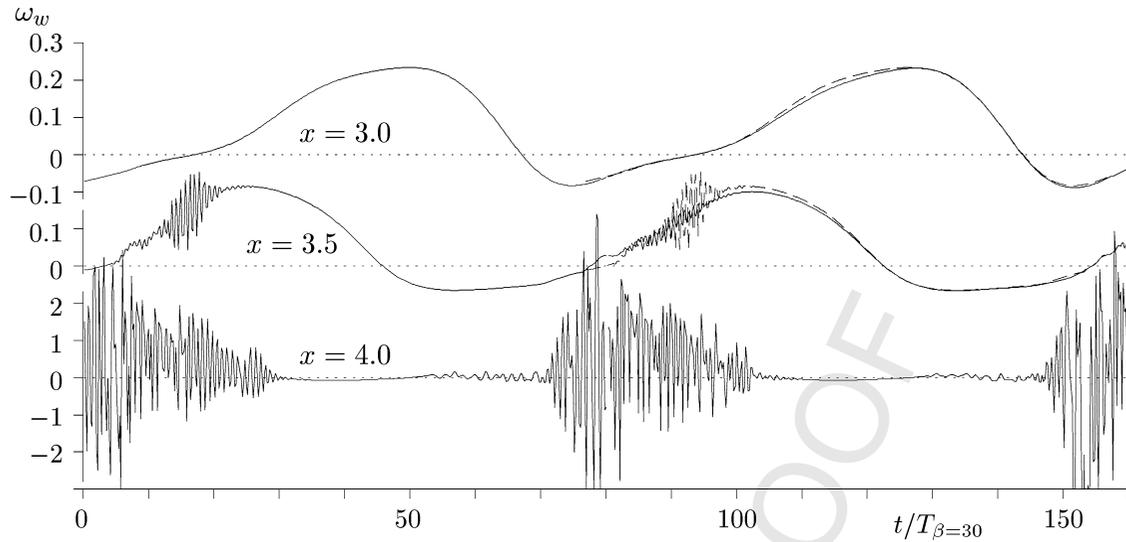
ARTICLE IN PRESS

S0997-7546(02)01205-0/FLA   AID:1205   Vol.●●●(●●●)
ELSGMLTM(EJMFLU):m4SC 2002/08/30 Prn:4/09/2002; 14:54   ejmflu1205   P.10 (1-15)
by:CG p. 10

10   *U. Rist, U. Maucher / European Journal of Mechanics B/Fluids* ●●● (●●●●) ●●●–●●●

Fig. 12. Time traces of vorticity at the wall at $x = 3.0$, 3.5, and 4.0 (top to bottom); note the different scale for $x = 4.0$.
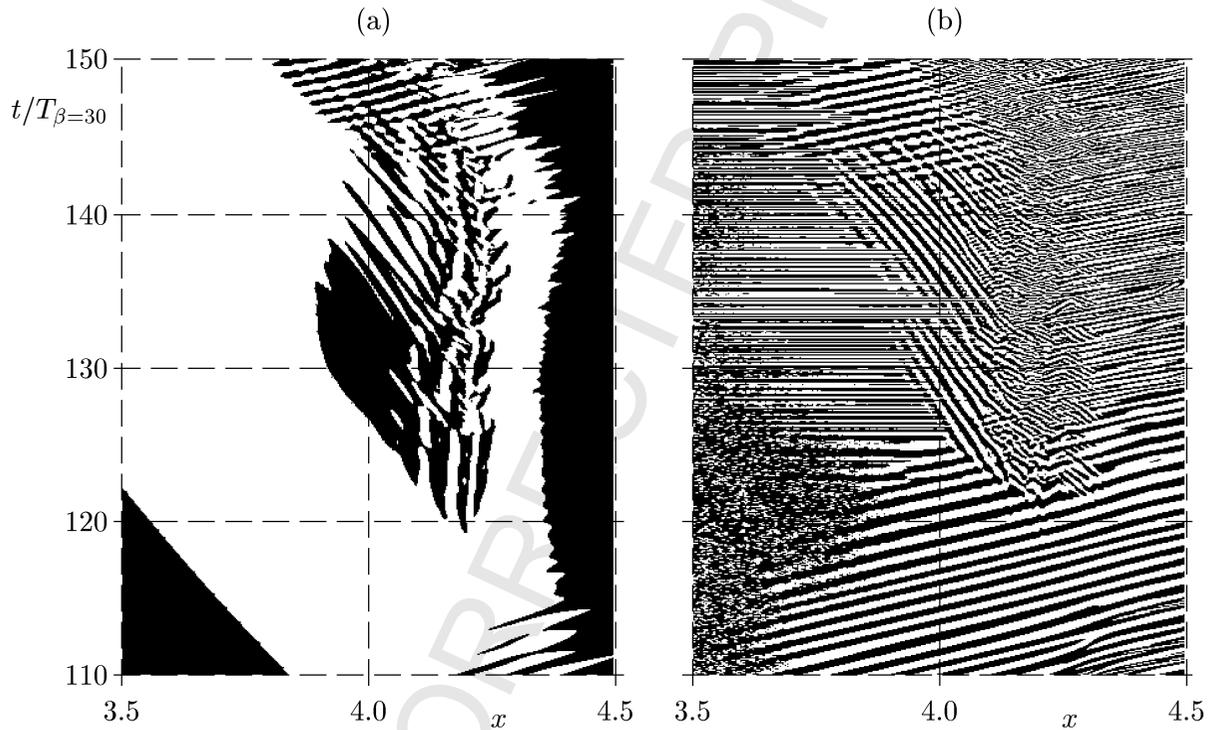

Fig. 13. x–t-diagram of ω_w (a) and $\partial^4 \omega_w / \partial t^4$ (b).

An excellent insight into the unsteady behaviour of the bubble and into the nature of unsteady small-amplitude disturbances can be obtained from x–t-diagrams of the wall vorticity ω_w, as well as its higher time derivatives $\partial^n \omega_w / \partial t^n$. Using a higher time derivative works like using a high-pass filter since it eliminates the low-frequency unsteadiness of the "mean flow" and magnifies the high-frequency disturbances, see Maucher et al. [24].

Fig. 13 examines the bubble and its disturbance behaviour in the region $3.5 \leqslant x \leqslant 4.5$ for the interval $110 \leqslant t/T_{\beta=30} \leqslant 150$ in subfigures (a) and (b), respectively. Attached flow (positive wall shear) is visualized in black while reverse flow areas are left white. Thus, the separation point in the lower left corner of the plot is seen to move upstream and to the outside of the region

ARTICLE IN PRESS

S0997-7546(02)01205-0/FLA   AID:1205   Vol.●●●(●●●)   ejmflu1205   P.11 (1-15)
ELSGMLTM(EJMFLU):m4SC 2002/08/30 Prn:4/09/2002; 14:54   by:CG p. 11

U. Rist, U. Maucher / European Journal of Mechanics B/Fluids ●●● (●●●●) ●●●–●●●   11

shown. Compared to this, the re-attachment point remains rather steady apart from some high-frequency disturbances which are emphasized by considering the fourth time derivative of the wall shear in Fig. 13(b). The streaks which appear in these figures represent disturbance paths. Several interesting features can be observed. For instance, downstream travelling waves (positive slope of the streaks) near the lower and upper borders of the figure, as well as for $x > 4.2$ for all times. However, the most interesting observation in the present context is the occurrence of streaks with *negative slope* which indicate upstream travelling waves in the center of the plot originating between $x \approx 4.1$ and $x \approx 4.3$. Compared to the downstream travelling waves these disturbances travel much slower. Horizontal lines indicate small-scale pressure fluctuations due to the elliptical nature of the incompressible flow.

In order to investigate a possible connection with the stability investigations of the first part of the present paper (Section 2), base flow profiles are extracted and analysed from the quasi-steady regime $110 \leqslant t/T_{\beta=30} \leqslant 120$ before the upstream-travelling disturbances appear. A comparison of the mean-flow profiles with instantaneous profiles in Fig. 14 shows that these are indeed quasi steady.

The parameterisation of the mean-flow profiles with respect to the parameters chosen for LST in Section 2 is shown in Fig. 15. Small irregularities arise from searching data on a discrete grid. The Reynolds number based on the displacement thickness reaches $Re_{\delta 1} \approx 3000$, the height of the reverse-flow region indicated by the point in the boundary layer where $u = 0$ and the reverse flow maximum attain 50% and 20%, respectively. Compared to the results of Section 2 this is not yet enough to cause a time-growing instability (based on our local analysis).

However, the temporal evolution of the maximal reverse flow and of the height parameters in Fig. 16 indicate that the absolutely unstable region found in Section 2 is entered with increasing time. The parameters for this plot have been normalized with a constant 'mean' displacement thickness and free-stream velocity in order to make processing of the data easier. As
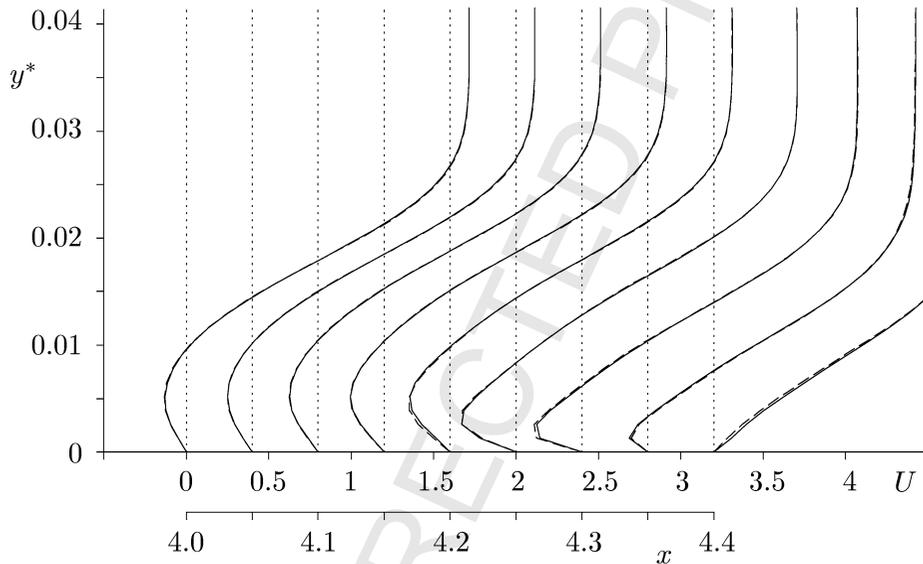

Fig. 14. Mean-flow profiles in the interval $115 \leqslant t/T_{\beta=30} \leqslant 120$ compared to instantaneous profiles $(--)$ at $t/T_{\beta=30} = 117.5$.
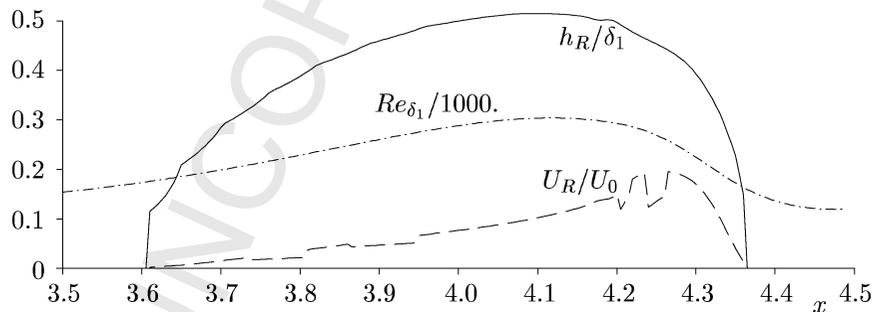

Fig. 15. Mean-flow parameters in the interval $115 \leqslant t/T_{\beta=30} \leqslant 120$.

ARTICLE IN PRESS

S0997-7546(02)01205-0/FLA   AID:1205   Vol.●●●(●●●)
ELSGMLTM(EJMFLU):m4SC 2002/08/30 Prn:4/09/2002; 14:54   ejmflu1205   P.12 (1-15)
by:CG p. 12

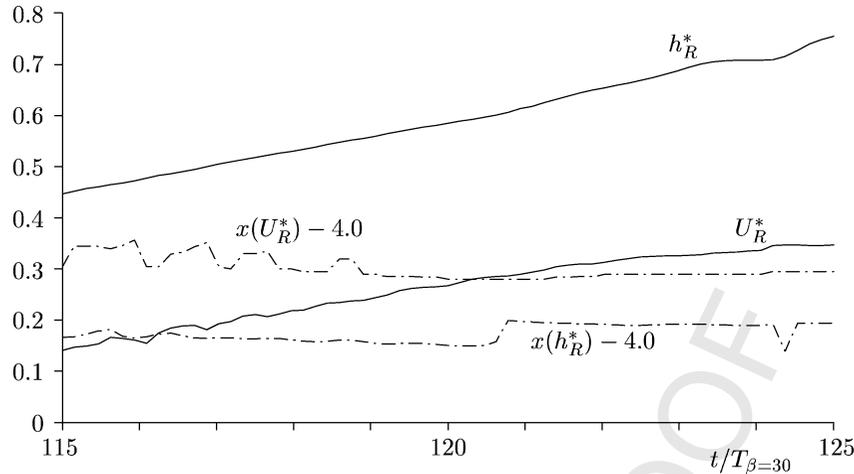12   *U. Rist, U. Maucher / European Journal of Mechanics B/Fluids ●●● (●●●●) ●●●–●●●*
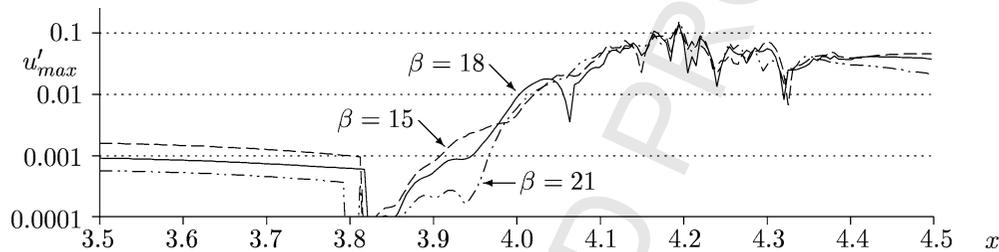
Fig. 16. Time evolution of mean-flow parameters.

Fig. 17. Disturbance amplitudes for three frequencies in the interval $130 \leqslant t/T_{\beta=30} \leqslant 140$.

indicated by their respective x-positions, maximal reverse flow and maximal height appear rather close to each other in the region $4.2 \leqslant x \leqslant 4.3$. Since the Reynolds number ($Re_{\delta_1}|_{max} \approx 3700$) has only a small influence on the instability in the present range its time evolution is not considered here.

According to Fig. 13 the time-growing instability sets in at $t/T_{\beta=30} \approx 121$. At this time $U_{R\,max} \approx 0.3$ and $h_{R\,max}/\delta_1 \approx 0.6$ as shown in Fig. 16. For these parameters our instability computations based on analytical base-flow profiles also indicate absolute instability (corresponding to the definition of Gaster [17]). In a diagram for $U_R = 0.3$ similar to Fig. 3(c) the temporal growth rate becomes greater than zero for all Reynolds numbers when $h_R/\delta_1 = 0.6$. The corresponding frequency is $\beta_{0,r} \cdot \delta_1 = 0.5$. This is exactly in the range $15 < \beta < 21$ observed in the DNS because it corresponds to $\beta = 20$ for $\delta_1 = 0.025$ which is actually observed.

In other words, Fig. 16 together with the parameter study performed in Section 2 indicates that upstream propagating disturbances can originate from a time-growing instability of the mean-flow profiles at $x \approx 4.2$–4.3 from where they travel upstream into the stable flow. This means that their amplitude should decay with increasing distance from the source while they grow in time for $x = const$. According insights into the high-frequency disturbances which develop out of the instability identified in the rearward part of the LSB are expected from a Fourier analysis of the instantaneous data in the interval $130 \leqslant t/T_{\beta=30} \leqslant 140$ which are presented in Figs. 17 and 18. A Hanning window has been used to reduce effects due to non-periodicity.

Basically, two distinct regions appear in the amplitude spectrum: the upstream part of the flow field is dominated by very low frequencies $\beta \to 0$ while in the downstream part a maximum develops in the region $15 \leqslant \beta \leqslant 21$. Fig. 17 displays amplitudes of the first maximum from the wall for the three dominant frequencies $\beta = 15$, 18, and 21. As can be seen, the border between the two areas lies in the vicinity of $x = 3.8$. The sudden drop to much lower amplitudes is due to showing the first maximum of the amplitude profiles away from the wall (for the complete amplitude profiles see Fig. 18(b). The low frequency disturbances in the upstream part slowly decay with x while those in the downstream part grow with x in a very rapid manner. Since we know already from the x–t-diagrams in Fig. 13 that the latter disturbances must travel upstream approximately in the region $3.8 < x < 4.2$ this is indeed identical to an upstream decay, as expected above.

The amplitudes and phases in Fig. 18 further document the nature of the different disturbances in the up- and downstream part. The phases which are drawn for a single frequency $\beta = 18$ and for three distances from the wall show three regions.
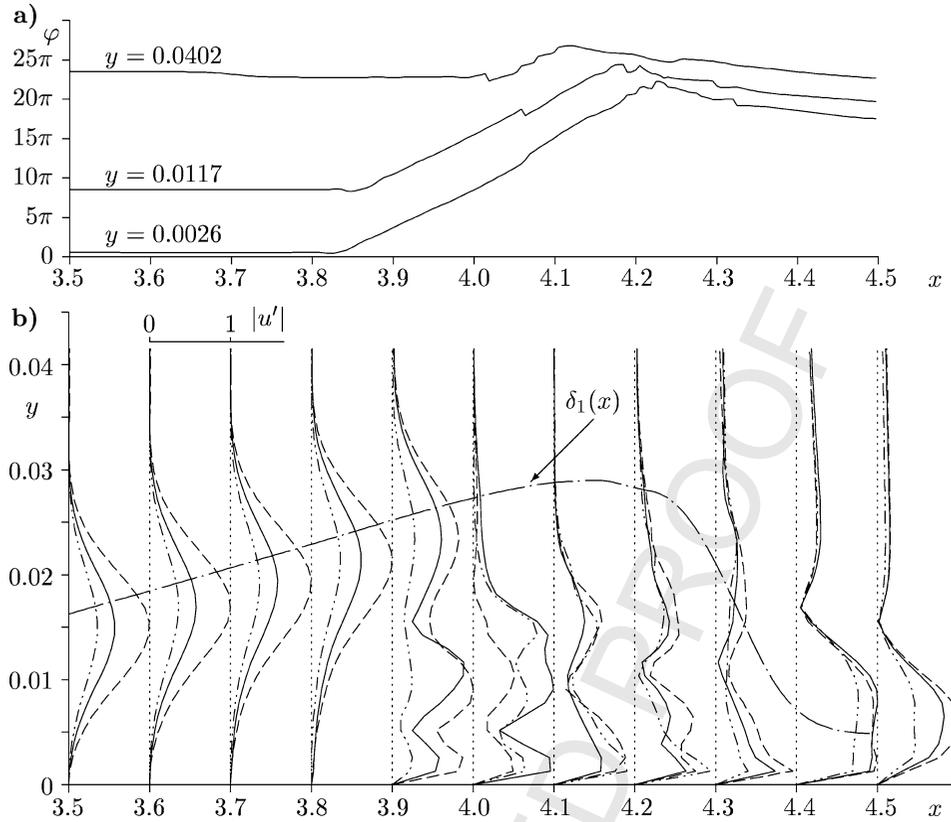
Fig. 18. Disturbance flow phases for frequency $\beta = 18$ (a) and amplitude profiles for frequencies $\beta = 15$ (– ·· –), 18 (——), and 21 (– –) (b) in the interval $130 \leqslant t/T_{\beta=30} \leqslant 140$. $\delta_1 =$ displacement thickness.

Constant phase in the upstream part of the figure, positive slope in the middle which represents upstream travelling waves, and negative slope for downstream travelling disturbances in the downstream part of the selected region. The region of upstream travelling disturbances is restricted to the central part of the bubble (cf. Fig. 11(c) for $t/T_{\beta=30} = 135$) but not exclusively linked to y-positions with reverse flow because $y = 0.0402$, for instance, is in the free-stream flow.

In Fig. 18(b) the disturbance amplitudes are presented again for the three frequencies $\beta = 15$, 18, and 21 which dominate the spectrum for $x > 3.85$. They are normalized to the maximum of the largest frequency for each x-station in order to document their relative importance with respect to each other. Their absolute amplitudes can be inferred from the amplitudes in Fig. 17. As already mentioned above, the lowest frequency exhibits the largest relative amplitude in the left part of the figure, i.e., for $x < 3.9$. The constant phase in this region together with the broad amplitude maxima vs. y and their close correlation with the wall-normal gradient of the mean flow indicate that these disturbances do not correspond to eigenoscillations of the flow but simply reflect the slowly changing base flow in this region similar to the 'wavering' of Spalart and Strelets [5]. With increasing x the mean-flow change occurs farther away from the wall because it is coupled to the growing wall distance of the separated boundary layer. Interestingly, the y-position of the maximum approximately follows the displacement thickness $\delta_1(x)$ of the mean flow.

At $x = 3.9$ the upstream travelling eigenoscillations due to the time-growing instability start to dominate. They are characterized by two maxima below the shear layer and a fast decay to negligible values for large y. The first maximum which is initially lower than the amplitude due to 'wavering' can be seen in Fig. 17 at $x < 3.9$. From there on it quickly grows to larger values than the 'wavering'. The following growth is approximately the same for all frequencies, but spatial amplitude variations occur, first for $\beta = 18$, later for all frequencies. These changes could indicate that the disturbances consist of several modes with different propagation velocities, that nonlinear effects are present, or that a Fourier analysis of the data is no longer able to convey the information. Despite this, the corresponding amplitude profiles in Fig. 18(b) indicate that the downstream travelling disturbances for $x > 4.2$ resemble the characteristic eigenfunctions of Tollmien–Schlichting waves: a large maximum near the wall, zero amplitude further away, a second maximum near the boundary layer edge, and a slow decay for $y \rightarrow \infty$. This is typical for a convectively unstable boundary layer, where unsteady disturbances lead to TS-waves (as long as the initial amplitude is not large enough to cause bypass transition).

ARTICLE IN PRESS

S0997-7546(02)01205-0/FLA   AID:1205   Vol.●●●(●●●)
ELSGMLTM(EJMFLU):m4SC 2002/08/30 Prn:4/09/2002; 14:54

ejmflu1205

P.14 (1-15)
by:CG p. 14

14   *U. Rist, U. Maucher / European Journal of Mechanics B/Fluids ●●● (●●●●) ●●●–●●●*

4. Conclusions

Predictions using LST helped to identify the influence of different parameters on a possible absolute instability of modelled base-flow profiles with reverse flow near the wall. Threshold values for the reverse flow already found in literature have been confirmed. In addition to earlier investigations, the influence of Reynolds number and wall distance of the detached shear layer, respectively its strength, have been investigated. The shape of the eigenfunctions of the wall-parallel velocity component helped to identify the contribution of viscous and inviscid mechanisms. For large wall distances two unstable modes have been identified which replace each other when the wall-distance of the shear layer is altered.

In the second part of the present investigations (Section 3) a time-growing instability could be identified in the 2-D DNS of a laminar separation bubble. For a certain time, disturbances generated in the reattachment zone amplify locally while they shed upstream travelling waves. The observation has been possible with the help of specially adapted signal analysis techniques and a very low disturbance environment upstream of the bubble. Compared to the predictions using LST in Section 2 there is a quite remarkable agreement between prediction and observation despite the nonlinear character of the disturbance development in the DNS.

Unfortunately, the amplitude profiles in Fig. 18(b) compare very badly with the eigenfunctions in Section 2 apart from the fact that the first maximum also occurs at $y/\delta_1 \approx 0.09$. This is in some contrast to the good agreement with the eigenvalues, namely, the parameters for onset of temporal growth and the value of the most unstable frequency. This could be due to several reasons. First, the present disturbances are non-linear because they are larger than 1% U_∞ for $x \geqslant 4.0$. Second, they seem to consist of a superposition of several modes with different phase speeds which leads to rapid changes of their Fourier amplitudes with x in a somewhat random way. Third, the disturbances discovered in the DNS travel upstream at a finite speed instead of $c_{gr} = 0$ as in the LST.

Nevertheless, a local analysis of the base-flow profiles at $x = 4.2$ in the interval $130 \leqslant t/T_{\beta=30} \leqslant 140$ was tried using the Orr–Sommerfeld matrix solver from Gmelin et al. [25]. The scheme is restricted to temporal amplification ($\alpha_i = 0$, $\beta_i \neq 0$) but by slowly adjusting α_r the solution was iterated to a given frequency β_r. Interestingly, for each of the three frequencies considered above an unstable eigenvalue was found with negative group velocity ($c_{gr} \approx -0.14$) and a rather close agreement of α_r with the DNS (extracted from plots like Fig. 18(a)). Moreover, the (approximate) spatial growth rate obtained from these eigenvalues by using the Gaster transformation $\alpha_i = \beta_i/c_{gr} \approx -42$ was in excellent agreement with the amplification observed in Fig. 17 in the region $x = 3.95\ldots4.0$, and the eigenfunctions resembled the profiles of the upstream propagating disturbances shown in Fig. 18(b). However, decreasing the x position of the base flow somewhat led to stable eigenvalues. Besides this, the eigenvalues of the matrix solver were very robust with respect to the wall-normal discretisation of the base flow, but they could not be confirmed using the shooting method used in Section 2. Strictly speaking, the good agreement of these eigenvalues with the DNS results might be fortuitous, because already a slight increase of the x position of the base-flow profile (by $\Delta x = 0.01$) led to unstable eigenvalues with much larger streamwise wave number, less amplification and smaller group velocity. Because of this critical non-parallel influence of the base-flow profile on the eigenvalues which cannot be eliminated, further results of LST are not presented here.

Despite these short-comings on the side of the stability theory applied, the final picture is that of upstream propagating disturbances originating from a time-growing instability of the mean-flow profiles at $x \approx 4.2$ which travel upstream into the stable flow, i.e., their amplitudes decay with decreasing x while they grow in time for $x = const$. Outside the region of temporal instability these unsteady oscillations generate Tollmien–Schlichting waves which dominate downstream of the bubble. As time evolves these downstream travelling waves are superimposed on the upstream travelling ones, see Fig. 13 at $t/T_{\beta=30} \geqslant 140$. Once the disturbances have grown to higher and higher amplitudes they influence the base flow in such a way as to move the re-attachment point upstream. The bubble moves upstream into the region of zero pressure gradient where it ceases to exist, until a new one is re-created further downstream in the region of the highest adverse pressure gradient. Conceptually, the reason for this low-frequency oscillation of the "mean flow" is clear, but further details need additional investigations.

References

[1] I. Tani, Low-speed flows involving bubble separations, Progr. Aeron. Sci. 5 (1964) 70–103.

[2] M. Gaster, The structure and behaviour of laminar separation bubbles, in: AGARD CP-4, Flow Separation, Part II, 1964, pp. 813–854.

[3] J.L. Van Ingen, Research on laminar separation bubbles at Delft University of Technology, in: V.V. Kozlov, A.V. Dovgal (Eds.), Separated Flows and Jets, IUTAM Symp. Novosibirsk/USSR, 1990, Springer-Verlag, Berlin, 1991, pp. 537–556.

[4] L.L. Pauley, P. Moin, W.C. Reynolds, The structure of two-dimensional separation, J. Fluid Mech. 220 (1990) 397–411.

[5] P.R. Spalart, M.K. Strelets, Mechanisms of transition and heat transfer in a separation bubble, Fluid Mech. 403 (2000) 329–349.

[6] Z. Yang, P.R. Voke, Large-eddy simulation of boundary-layer separation and transition at a change of surface curvature, J. Fluid Mech. 439 (2001) 305–333.

[7] M. Gaster, Stability of velocity profiles with reverse flow, in: M.Y. Hussaini, A. Kumar, C.L. Streett (Eds.), Instability, Transition and Turbulence, ICASE-Workshop, Springer-Verlag, Berlin, 1991, pp. 212–215.

[8] T. Allen, N. Riley, Absolute and convective instabilities in separation bubbles, Aeron. J. Roy. Aeron. Soc. (December 1995) 439–448.

[9] A. Michalke, On the inviscid instability of wall-bounded velocity profiles close to separation, ZFW 14 (1990) 24–31.

[10] D.A. Hammond, L.G. Redekopp, Local and global instability properties of separation bubbles, Eur. J. Mech. B Fluids 17 (1998) 145–164.

[11] M. Alam, N.D. Sandham, Direct numerical simulation of 'short' laminar separation bubbles with turbulent reattachment, J. Fluid Mech. 410 (2000) 1–28.

[12] J.H. Watmuff, Evolution of a wave packet into vortex loops in a laminar separation bubble, J. Fluid Mech. 397 (1999) 119–169.

[13] U. Rist, U. Maucher, Direct numerical simulation of 2D and 3D instability waves in a laminar separation bubble, in: AGARD CP-551, Application of Direct and Large Eddy Simulation to Transition and Turbulence, Chania, Crete, 1994, pp. 34-1–34-7.

[14] U. Rist, U. Maucher, S. Wagner, Direct numerical simulation of some fundamental problems related to transition in laminar separation bubbles, in: J.-A. Désidéri, C. Hirsch, P. Le Tallec, M. Pandolfi, J. Périaux (Eds.), Computational Fluid Dynamics '96, Wiley, 1996, pp. 319–325.

[15] V. Maucher, Numerische Untersuchungen zur Transition in der laminaren Ablöseblase einer Tragflügelgrenzschicht, Dissertation Universität Stuttgart, 2001.

[16] F.M. White, Viscous Fluid Flow, McGraw-Hill, New York, 1974.

[17] M. Gaster, Growth of disturbances in both space and time, Phys. Fluids 11 (4) (1968) 723–727.

[18] U. Maucher, U. Rist, S. Wagner, Transitional structures in a laminar separation bubble, in: W. Nitsche, H.J. Heinemann, R. Hilbig (Eds.), New Results in Numerical and Experimental Fluid Mechanics II, NNFM, Vol. 72, Proc. 11th STAB/DGLR-Symposium, Berlin, November 10–12, 1998, Vieweg, Braunschweig, 1999, pp. 307–314.

[19] U. Maucher, U. Rist, M. Kloker, S. Wagner, DNS of laminar-turbulent transition in separation bubbles, in: E. Krause, W. Jäger (Eds.), High Performance Computing in Science and Engineering '99, Springer-Verlag, Berlin, 2000, pp. 279–294.

[20] U. Rist, H. Fasel, Direct numerical simulation of controlled transition in a flat-plate boundary layer, J. Fluid Mech. 298 (1995) 211–248.

[21] K. Gruber, H. Bestek, H. Fasel, Interaction between a Tollmien–Schlichting wave and a laminar separation bubble, AIAA Paper 87-1256, 1987.

[22] M. Kloker, U. Konzelmann, H. Fasel, Outflow boundary conditions for spatial Navier–Stokes simulations of transitional boundary layers, AIAA J. 31 (1993) 620–628.

[23] U. Maucher, U. Rist, S. Wagner, Direct numerical simulation of airfoil separation bubbles, in: S. Wagner, E.H. Hirschel, J. Périaux, R. Piva (Eds.), Computational Fluid Dynamics '94, Wiley, 1994, pp. 471–477.

[24] U. Maucher, U. Rist, S. Wagner, A method for the identification of high-frequency oscillations in unsteady flows, Z. Angew. Math. Mech. 77 (1) (1998) S209–S210.

[25] C. Gmelin, U. Rist, Active control of laminar-turbulent transition using instantaneous vorticity signals at the wall, Phys. Fluids 13 (2) (2001) 513–519.